LETTER

Remote Molecular Doping of Colloidal Quantum Dot Photovoltaics

Ahmad R. Kirmani,[†] Amirreza Kiani,[‡] Marcel M. Said,[§] Oleksandr Voznyy,[‡] Nimer Wehbe,[†] Grant Walters,[‡] Stephen Barlow,[§] Edward H. Sargent,[‡] Seth R. Marder,[§] and Aram Amassian*,[†]

[†]King Abdullah University of Science and Technology (KAUST), KAUST Solar Center (KSC), and Physical Science and Engineering Division (PSE), Thuwal 23955-6900, Saudi Arabia

[‡]Department of Electrical and Computer Engineering, University of Toronto, Toronto, Ontario M5S 3G4, Canada

[§]School of Chemistry and Biochemistry and Center for Organic Photonics and Electronics, Georgia Institute of Technology, 901 Atlantic Drive, Atlanta, Georgia 30332-0400, United States

ⓢ *Supporting Information*

ABSTRACT: In recent years colloidal quantum dot (CQD) photovoltaics have developed rapidly because of novel device architectures and robust surface passivation schemes. Achieving controlled net doping remains an important unsolved challenge for this field. Herein we present a general molecular doping platform for CQD solids employing a library of metal−organic complexes. Low effective ionization energy and high electron affinity complexes are shown to produce n- and p-doped CQD solids. We demonstrate the obvious advantage in solar cells by p-doping the CQD absorber layer. Employing photoemission spectroscopy, we identify *two doping concentration regimes*: lower concentrations lead to efficient doping, while higher concentrations also cause large surface dipoles creating energy barriers to carrier flow. Utilizing the lower concentration regime, we remove midgap electrons leading to 25% enhancement in the power conversion efficiency relative to undoped cells. Given the vast number of available metal−organic complexes, this approach opens new and facile routes to tuning the properties of CQDs for various applications without necessarily resorting to new ligand chemistries.
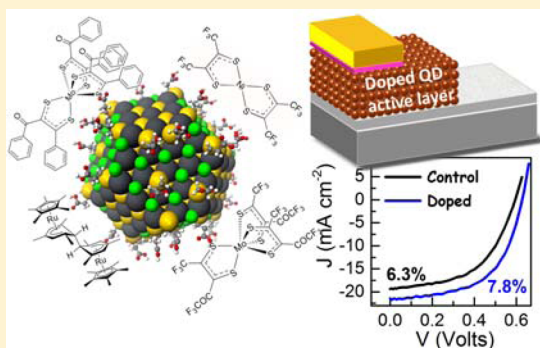
Colloidal quantum-dot (CQD) optoelectronics and photovoltaics have seen advancement ever since the demonstration of facile and scalable routes to nanocrystal synthesis in the early 1990s.[1−3] The possibility of achieving >100% external quantum efficiency (EQE), coupled with band gap tunability, make CQDs a promising prospect for photovoltaics.[4−9] Recent demonstrations of air-stable CQD solar cells are compatible with roll-to-roll manufacturing techniques such as spray-coating and have brought this technology a significant step closer to commercial implementation.[10−13] CQD photovoltaics have recently shown both efficient device architectures and fruitful deployment of robust passivation schemes.[2,3,5,7,10,11,14]

The large surface-to-volume ratio of QDs leads to surface-related charge trapping that limits device performance.[15−24] Surface ligand exchange through chemical routes has traditionally served the important purpose of passivating surface traps and bringing the QDs closer for increased electronic coupling.[25] Among ligand-exchange routes, solid-state ligand exchange is the most commonly implemented approach to passivate QDs and improve film conductivity for solar cell applications.[19,26,27]

Achieving controlled passivation and net doping of CQD solids without resorting to, or being limited by, chemical routes remains an important and largely unsolved challenge for this field. The capability to tune the net doping without the burden of redesigning the processing and chemistry of CQD film fabrication will greatly enhance the ability to tailor the electronic properties of CQD solids. Remote doping is a versatile strategy that does not interfere with QD surface chemistry, interdot spacing, and film order at the nanoscale. It is free from steric hindrance and can complement existing solution and solid-state ligand-exchange schemes. The observation of remote electron transfer by Shim and Guyot-Sionnest in CdSe QDs opened the door to realizing successful doping schemes in QDs without resorting to chemical modification of QD surfaces.[28] Recently, Konstantatos and co-workers demonstrated remote passivation of in-gap trap states by introducing ZnO nanocrystals into the CQD solid, leading to suppression of trap-assisted carrier recombination.[29]
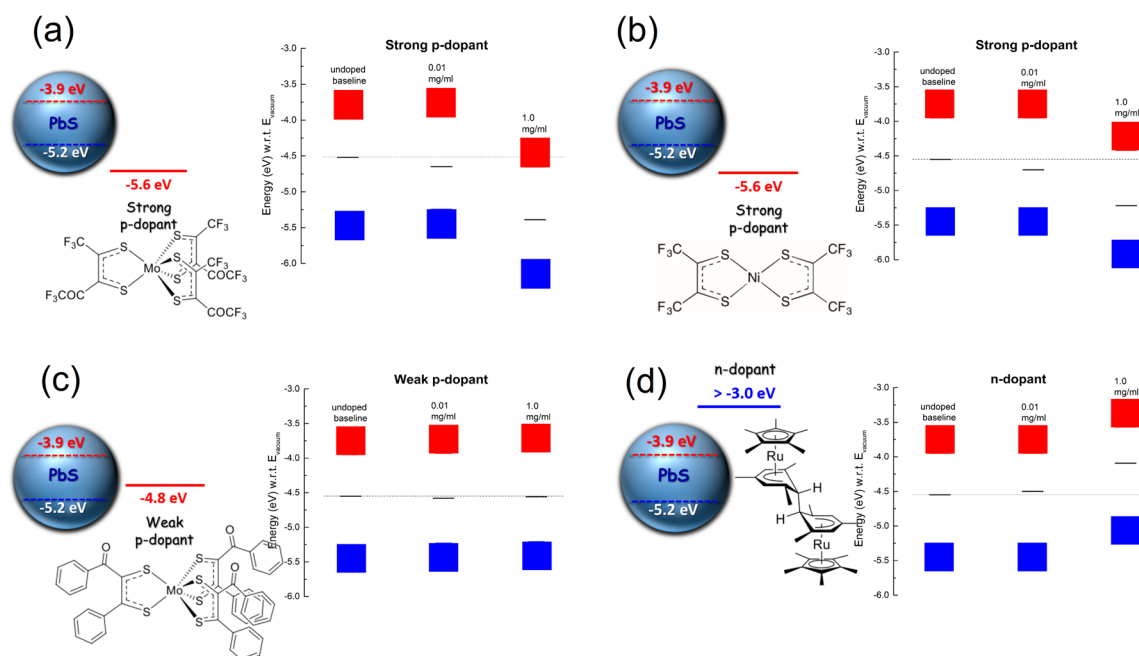
Figure 1. General molecular doping platform for CQD solids. The doping scenarios examined in this study are demonstrated. The estimated EA (red) and effective IE (blue) molecular levels are shown corresponding to each dopant relative to the energetics of the QD. (a) Mo(tfd-COCF$_3$)$_3$ and (b) Ni(tfd)$_2$ are expected to behave as strong p-dopants because of their deep EA, compared to the band structure of CQDs. (c) Mo(PhBz-dt)$_3$, with a shallower EA, behaves as a weak p-dopant. (d) (RuCp*mes)$_2$ is a strong n-dopant having a low effective IE. These expectations are largely verified by UPS measurements which show relevant changes to the band structures. The weak p-dopant shows a negligible shift to the Fermi level, while the strong dopants generally cause major shifts to the Fermi level. Importantly, these Fermi level changes are associated with corresponding shifts in the Pb 4f core levels, as evidenced by XPS (Figure S1). Significant changes to the vacuum level (dipole formation) are observed when the CQD solids are treated with high concentrations of the dopants (1 mg mL^{-1}).

We took the view that a single-step, postdeposition remote doping protocol that can treat CQD solids could be a robust and highly desirable platform for enabling the controlled net doping of CQD solids for a wide gamut of applications. We demonstrate that soluble molecular dopants with carefully selected energetics and sufficiently small size infiltrate and dope PbS CQD solids. The remote doping is achieved in a single step without altering the deposition and exchange protocols of the CQD solid, making this a highly versatile scheme. We consider a variety of doping scenarios by employing a library of metal—organic complexes with different energetics [electron affinity (EA) and ionization energy (IE)]. Deep EA complexes (oxidants) are found to shift the Fermi level of the CQD solids toward the valence band edge, as evidenced by ultraviolet photoemission spectroscopy (UPS), indicating p-doping. Reductants with low effective IEs result in n-doping of the solids; however, the shift of the Fermi level for this case is minor. Employing UPS, we find that the lower concentrations lead to efficient electron removal and addition, while higher concentrations also result in significant surface-dipole formation. The facile procedure involves soaking the CQD solid in the dopant solution. The benefits of this solid-state remote doping scheme are demonstrated in the context of depleted heterojunction CQD solar cells, where p-doping of the CQD absorber layer effectively removes midgap electrons and suppresses traps. This renders the absorber layer substantially intrinsic and leads to a ca. 25% enhancement in power conversion efficiency (PCE) over the reference case. Our demonstration proves facile and scalable control of carrier concentration and in-gap trap states in CQD solids. Given the vast variety of available organic and metal—organic dopants, it

opens new and facile routes to tuning the properties of CQD solids for photovoltaics, optoelectronics, and other applications.

We begin by presenting the various doping scenarios examined in the study and the associated changes to the CQD bandstructures (Figure 1). We chose three metal—organic complexes having deep EA (p-dopants) and an organometallic dimer with shallow effective IE (n-dopant) with respect to the QD energetics. Schematics represent the energetics of the molecules and the CQD solids and the chemical structures of the various molecules involved. The doping procedure involved briefly soaking the CQD layer in a solution of dopant and acetonitrile (ACN). ACN was chosen as the solvent based on previous results which suggest that ACN, being aprotic and a high-dipole-moment solvent, is benign to the ligands on the QD surface.[19,30] The standard protic solvent, MeOH introduces in-gap trap states over prolonged exposure to QDs by leaching off the surface chloride atomic ligand. The molecule represented in Figure 1a, molybdenum tris(1-(trifluoroacetyl)-2-(trifluoromethyl)ethane-1,2-dithiolene), Mo(tfd-COCF$_3$)$_3$,[31,32] is a more soluble variant of molybdenum tris(1,2-bis(trifluoromethyl)ethane-1,2-dithiolene), Mo(tfd)$_3$, which has been successfully used to dope the hole-transporting material (HTM) N,N'-di-[(1-naphthyl)-N,N'-diphenyl]-1,1'-biphenyl-4,4' diamine, (α-NPD), via coevaporation in ultrahigh vacuum.[33] The high electron affinity (estimated to be >5.6 eV) makes it an oxidizing agent; therefore, the conductivity enhancement was attributed to compensation of trap states and contribution of free carriers by hole-injection from the dopant. Nickel bis(1,2-bis(trifluoromethyl)ethane-1,2-dithiolene), Ni(tfd)$_2$ (Figure 1b), has a reduction potential of +0.33 V vs FeCp$_2^{+/0}$;[34] although its solid-state EA has not been directly measured, comparison of its electrochemistry with that
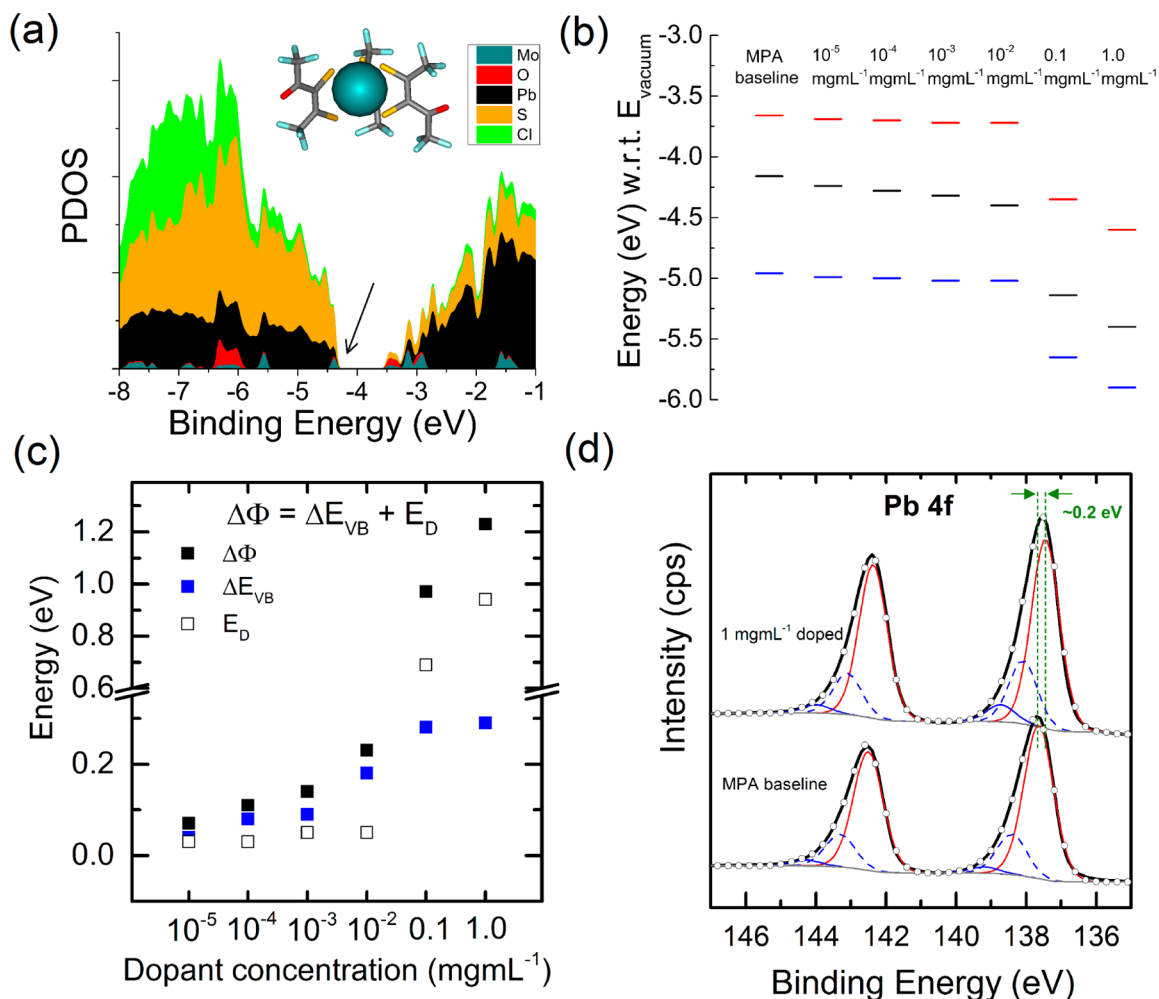
Figure 2. (a) Results of DFT simulations that yield a picture qualitatively similar to that estimated from experiment, in which the molecule's LUMO (depicted by the black arrow) occurs at an energy similar to the VBM of the QDs, opening the possibility of the depopulation of the midgap or VB electrons, depending upon the dopant concentration, via remote doping. (b) Photoemission spectroscopy data for PbS QD films treated with solutions of varying dopant concentrations. VB edges (blue) and Fermi levels (black) were acquired using UPS while the conduction band edges (red) were estimated by adding the optical band gap (1.3 eV) to the VB energy. This is justified in the current case because the exciton binding energy (BE) for PbS QDs is low (~0.09 eV). For low doping concentrations, the Fermi level is found to shift moderately toward the VB, indicating midgap electron transfer. Higher doping concentrations, however, lead to valence electron transfer and surface dipole formation causing a significant lowering of the vacuum level and Fermi level relative to vacuum. The energies of the dipoles formed (E_D) are extracted from these results and shown in panel c. The Pb 4f core level peak, obtained from high-resolution XPS, is shown in panel d for the MPA baseline and the maximum doping cases. The red component of the peak corresponds to the Pb bonded to S atoms in the QD. The dashed blue component is the Pb bonded to the MPA ligand, while the solid blue component is the tiny amount of Pb−O. The peak shows a ca. 0.2 eV shift to lower binding energy for the maximum doping concentration, which is commensurate with the Fermi level shift observed for that concentration due to electron transfer (ΔE_{VB} in panel c).

of Mo(tfd)$_3$ suggests an EA of ca. 5.6 eV,[35] sufficiently oxidizing that it acts as p-dopant, accepting electrons from the CQDs (Figure 1a). Molybdenum tris(1-phenyl-2-benzoyl-1,2-dithiolene), Mo(PhBz-dt)$_3$, on the other hand, is much less oxidizing (−0.38 eV, which comparing to Mo(tfd)$_3$ corresponds to an EA of ca. 4.9 eV) and should therefore act as a weaker p-dopant (Figure 1c). Ruthenium (pentamethylcyclopentadienyl) (mesitylene) dimer, (RuCp*mes)$_2$, is a strong n-dopant (Figure 1d) with effective potential for the monomer cation/neutral dimer redox couple of ca. −2.0 V vs FeCp$_2^{+/0}$,[36] roughly corresponding to an effective solid-state IE of <3.0 eV.[37]

We sought to probe bandstructure changes that might give experimental evidence of electron transfer. We used UPS, a direct probe of electronic bandstructure, the density of states below the Fermi level (E_F) of a material, widely used to study

the effects of changes to nanomaterial surfaces on their band structures.[18,19,38,39] Miller et al. have recently highlighted the challenges associated with UPS measurements on larger size QDs which exhibit a small band gap, owing to the extremely low density of states at the valence band maximum.[40] However, the CQDs considered in our work have a larger band gap because they are small-size particles; hence, the UPS results are expected to be reliable, commensurate with the findings of Miller and co-workers.

Direct evidence of an electron transfer in doped MoS$_2$ films has recently been reported by Tarasov et al. where a shift in the E_F was observed and ascribed to transfer of electrons and holes.[41] This shift corresponded to a similar shift in the Mo core level peak measured by X-ray photoelectron spectroscopy (XPS). QD films obtained via spin coating were treated with
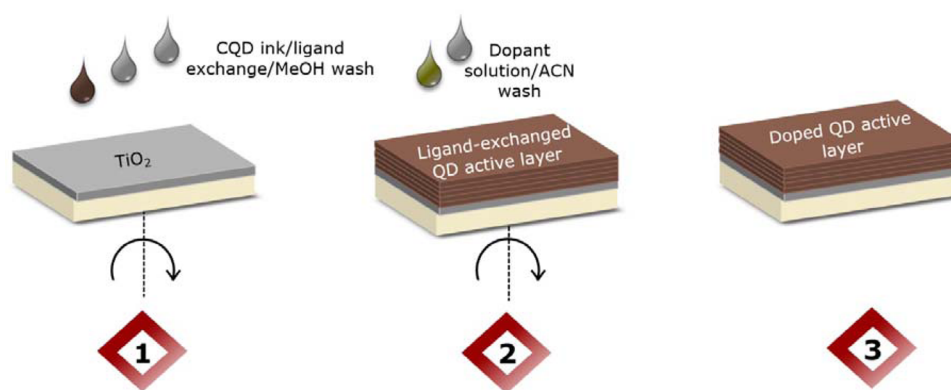
Figure 3. Procedure of molecular doping demonstrated in this study. (1) LbL deposition of the QD absorber layer via spin coating involves sequential deposition of CQDs (capped with oleic acid ligands) followed by solid-state ligand exchange with MPA and a subsequent methanol (MeOH) washing step. This cycle was repeated typically 10 times until the targeted film thickness (∼300 nm) was achieved. (2) The film was soaked in the dopant solution (dissolved in acetonitrile, ACN) for an optimized time duration before spinning off the excess solution. This was followed by a rinsing step in ACN to wash off any residual dopant and dry the sample (3) for use in subsequent solar cell fabrication steps.

various concentrations of the dopant solution to track changes to the band structure. Corresponding to the schematics in Figure 1 are the band strutures of the doped CQDs as measured by UPS. Each set shows *three* scenarios: undoped CQD baselines, CQDs doped with low-concentration dopant solution, and CQDs doped with high-concentration dopant solution. The effect of doping on the band structures can be broadly categorized into two regimes: *smaller doping concentrations* lead to changes of the Fermi level, which moves toward the valence band for p-doped films and toward the conduction band for n-doped films, *while higher doping concentrations* also result in changes to the vacuum level. A more detailed discussion of these two doping regimes will be done later. The observation of Pb 4f core level shifts from XPS corresponds to the electron transfer as a result of doping (Figure S1). We did not observe any new chemical components in the Pb or S core level peaks of the doped CQDs that might give an indication of a chemical interaction of the dopants with the CQDs, confirming this to be remote doping.

The fact that we observe effective p-doping of the CQD solids is of interest for solar cells in which the CQD solid is employed as the absorber layer. These absorber layers, which form a heterojunction with an n-type metal oxide (for example, titania) have been recently suggested to be slightly n-type.[42] We therefore took the view that a postsynthesis p-doping step should make the absorber layer more intrinsic, leading to extension of the depletion region into the CQD solid, eventually enhancing the solar cell performance. Encouraged by the successful deployment of $Mo(tfd)_3$ as a strong p-dopant for α-NPD, we chose the nonsymmetrical $Mo(tfd\text{-}COCF_3)_3$ (ca. 0.11 V more oxidizing than $Mo(tfd)_3$ in solution[32]) discussed in brief earlier (Figure 1a). The enhanced solubility of $Mo(tfd\text{-}COCF_3)_3$ makes it compatible with solution processing and therefore better suited for scalable manufacturing of CQD solids and devices thereof. We carried out a more in-depth study of the scenario of CQD solid p-doped with $Mo(tfd\text{-}COCF_3)_3$. The orbital energies for isolated $Mo(tfd\text{-}COCF_3)_3$ were calculated using density functional theory (DFT) and are shown in Figure S2.

DFT simulation of the energetics at the interface of this system supports the possibility of remote charge transfer. The results are shown in Figure 2a. Hybrid ligand-exchanged QDs (involving a solid-state exchange with 3-mercaptopropionic acid

ligand, MPA, and Cl)[43] were considered for these calculations. The density of states (DOS) corresponding to Mo belongs to the dopant. The results show a close proximity of the dopant's LUMO with the VBM of the QDs. This suggests the possibility that the dopant can extract midgap or valence electrons from the QDs via electron transfer.

In Figure 2b we show the electronic bandstructures of the QD solids for the various doping scenarios. The band structures remain almost unchanged for lower doping concentrations, while significant changes are observed for higher concentrations (UPS spectra are shown in Figure S3). The total change in the work function of a doped QD film (compared to the undoped, MPA baseline), denoted $\Delta\phi$, comprises the *Fermi level shift with respect to the VBM* owing to remote electron transfer (ΔE_{VB}) and the shift in the vacuum level due to *dipole formation on the QD surface* (E_D). This allows us to determine the energies E_D for the various doping scenarios (Figure 2c). We find that as the doping concentration increases, the surface dipole strengthens. This can be expected because, for 1.0 mg mL^{-1} doping concentration, each QD is surrounded by ca. 12 dopant molecules, as found from XPS atomic quantification (see Table S1 and the associated discussion). This drops to ca. 0.3 dopants per QD for 10^{-2} mg mL^{-1} dopant concentration, which agrees with the negligible value of E_D for this case (Figure 2c). We propose that the interface−dipole effects originate at the surface of each QD as a result of dopant penetration through the nanoscale voids in the QD solid, rather than being localized at the surface of the QD film; we do not observe any accumulation of the dopants on the film surface, as evidenced from secondary ion mass spectrometry (SIMS), even for the largest concentrations (Figure S4). The large $\Delta\phi$ values for this regime also involve a significant ΔE_{VB} hinting toward removal of valence electrons. For smaller concentrations, changes in ϕ are largely associated with changes to E_F from midgap electron transfer (Table S2). In this regime a significant shift in E_F relative to E_{VBM} requires fewer dopants than when the Fermi level approaches the band edge; therefore, the resultant interface dipole is relatively small. We also observe a ca. 0.2 eV shift of the Pb 4f core level peak (for 1.0 mg mL^{-1} doping concentration) towards the lower binding energy compared to an undoped QD solid, which can be ascribed to the downward shift of the Fermi level associated with p-doping (Figure 2d).[41] Core level shifts were observed for other
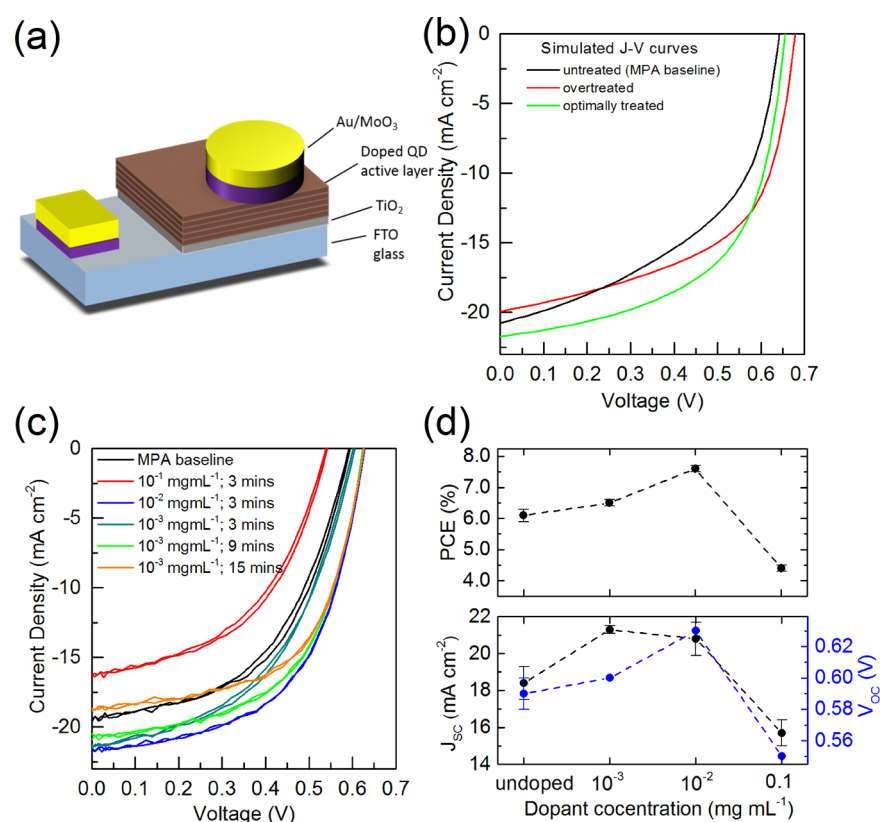
Figure 4. (a) Schematic of the depleted heterojunction (DHJ) device architecture employed in this study. (b) Simulated $J-V$ curves showing an increase in overall performance enhancement for solar cells made using optimally doped CQD films. Overdoped films show a performance decrease. (c) $J-V$ curves for solar cells made using CQD films treated with various doping concentrations and treatment times. (d) Averaged device parameters (PCE, J_{SC}, and V_{OC}) are shown as a function of the doping concentration for a soaking time of 3 min. The data highlight that 10^{-2} mg mL^{-1} is the optimized doping concentration for achieving best-performing devices.

Table 1. Summary of the Device Parameters for the Various Doping Scenarios[a]

device	soaking time (mins)	J_{SC} (mA/cm^2)	V_{OC} (V)	FF (%)	PCE (%)	R_{shunt} (kΩ/cm^2)	R_s (Ω/cm^2)
MPA baseline		18.4 ± 0.9	0.59 ± 0.01	55.6 ± 3.1	6.1 ± 0.2 (6.3)	1.98	8.0
10^{-3} mg mL^{-1}	3	21.3 ± 0.2	0.60 ± 0.00	50.4 ± 1.2	6.5 ± 0.1 (6.7)	3.49	6.8
	6	19.9 ± 0.9	0.62 ± 0.00	53.9 ± 0.5	6.7 ± 0.3 (6.9)	3.41	5.5
	9	20.1 ± 0.4	0.63 ± 0.00	59.5 ± 1.6	7.5 ± 0.1 (7.6)	4.78	4.9
	15	17.9 ± 0.5	0.63 ± 0.00	60.7 ± 1.5	6.8 ± 0.2 (6.9)	4.21	5.1
10^{-2} mg mL^{-1}	**3**	**20.8 ± 0.9**	**0.63 ± 0.00**	**58.3 ± 0.7**	**7.6 ± 0.1** (7.8)	**6.29**	**5.1**
	4	18.0 ± 0.6	0.60 ± 0.00	53.1 ± 2.3	5.8 ± 0.2 (5.9)	2.78	7.7
0.1 mg mL^{-1}	3	15.7 ± 0.7	0.55 ± 0.00	51.2 ± 2.1	4.4 ± 0.1 (4.5)	5.89	8.2

[a]The reported device parameters (J_{SC}, V_{OC}, FF, and PCE) have been averaged over 5−10 devices. The PCE values in parentheses represent the best-performing solar cells for each category.

concentrations as well and agreed with the accompanying Fermi level shifts.

While photoelectron spectroscopies are near-surface measurements, we confirm the dopant infiltrates the bulk of the CQD solid by SIMS measurements (Figure S4). Despite this infiltration, the dopant does not alter the interdot spacing, as demonstrated by grazing incidence small-angle X-ray scattering (GISAXS) (Figure S11). Consistent with the GISAXS data, no observable change in the overall film thickness was observed following doping, confirming the CQD solid is not swollen by infiltration of dopant molecules (Figure S6).

Having gained sufficient fundamental insights into the remote electron transfer from the QDs to Mo(tfd-COCF$_3$)$_3$ throughout the bulk of the CQD solid, we were interested in studying its effects on solar cell performance. The doping

strategy adopted successfully is outlined in Figure 3. The standard procedure of layer-by-layer (LbL) fabrication of the CQD absorber film was followed with the difference that the final CQD film was dipped in the dopant solution for an adjusted time before removal of the solution and solvent washing. An alternative doping scheme (not shown here; please refer to Figure S5 for a detailed explanation) wherein every layer in the LbL stack was individually doped failed to show performance enhancement (Figure S5 and Table S3), most likely due to overdoping of the film.

On the basis of the experimental and computational insights provided in Figure 2, we simulate the solar cell performances for undoped, optimally doped, and overdoped CQD absorber layers. An untreated MPA film was modeled as n-type with a doping concentration of 3×10^{16} cm^{-3}.[44,45] The optimally

treated film was modeled as either graded doped from 3×10^{16} cm^{-3} p-type in the last layer to 0 near the TiO$_2$ interface or 1×10^{16} cm^{-3} p-type homogeneously throughout, while the overtreated films were considered either as 3×10^{16} cm^{-3} throughout or graded doped from 1×10^{17} cm^{-3} to 0, leading to similar results. The simulated $J–V$ curves are shown in Figure 4b and suggest that doping leads to V_{OC} improvement due to the movement of the Fermi level closer to the band edge. Overdoping, however, collapses the depletion region leading to loss of J_{SC} and hence the overall device performance (for details, see Figure S7). While these simulations make certain assumptions and simplifications, they suggest that remote molecular doping should influence the performance of CQD solar cells.

In Figure 4c we show the experimentally measured $J–V$ curves for various doping concentrations. The device parameters are summarized in Table 1. It is evident that the device performance increases for low doping concentrations, whereas higher concentrations lead to performance degradation.

We observe device performance enhancement for solar cells soaked in low doping concentrations (10^{-3} mg mL^{-1}). Performance is found to increase with longer soaking times. However, an extended soaking (15 min) leads to decrease in device performance, an effect we ascribe to overdoping of the CQDs. Next, we test devices with higher doping concentrations (10^{-2} mg mL^{-1}) and achieve the maximum performance boost for a 3 min soaking time. The PCE of 7.8% obtained for this doping condition is a ca. 25% enhancement over the undoped baseline. We observe that at this elevated doping concentration, overdoping occurs at only 4 min of soaking leading to performance degradation. Doping the absorber layers with a high concentration (0.1 mg mL^{-1}) leads to immediate over-doping of the CQD solid and hence poorly performing solar cells. These experiments indicate that doping with an ACN solution can be effectively carried out in a single step in contrast to the repetitive ligand-exchange steps involved in the QD solid fabrication. The soaking in dopant solution allows the dopants to penetrate and diffuse into the entire QD film, as indicated by SIMS measurements (Figure S4). The optimized doping time and dopant solution concentration pair allows for the optimal dopant concentration levels to be found for any given QD solid. This is highlighted in Figure 4d where the various device parameters are plotted as a function of doping concentration for a soaking time of 3 min. The evolution of the device parameters, under illumination and in the dark, for the undoped control and the optimally doped solar cells is shown in Figure S14. The devices show photostability; however, they are found to degrade over a period of several weeks of storage. Importantly, doped devices do not degrade at a faster pace than the control undoped devices.

The shunt resistance, R_{shunt}, for all the better-performing doped devices is higher relative to the undoped controls, which provides evidence for the suppression of trap-assisted carrier recombination.[29] We suggest that the large surface dipoles introduced in conditions of higher doping concentration and the associated valence electron removal, as evidenced by UPS, lead together to the formation of localized energy barriers to efficient charge transport, causing performance degradation. In fact, we observe no change in the absorption of the QD solids (Figure S12) for nearly all doping conditions with the exception of 1.0 mg mL^{-1}, which shows evidence of exciton quenching.[46] Expectedly, a similar quenching is observed in the

transient absorption measurements for the highest doped solid (Figure S13), while no changes are observed in the carrier dynamics. These observations agree with the scenario of valence band electron removal at high doping concentrations, as discussed above. This is also supported by a quenching of the photoluminescence signal at the exciton energy (see Figure S10). Hence, only in-gap electron removal through ultralow doping of the QD solid leads to PV performance enhancements.

The absorber layer thickness in the solar cells reported above is ca. 300 nm, which consists of a ca. 250 nm depletion region.[45,47] In general, doping of the depletion region would lead to a decrease in the depletion width and hence in the solar cell performance. However, this would not occur if the undoped MPA-capped QD solid behaves as an n-type semiconductor. Indeed, as shown recently, the Fermi level of the MPA-capped QD solid lies slightly above midgap,[42] and as such the doping step makes the absorber layer more intrinsic via p-doping, instead of leading to a depletion region collapse. We further tested this hypothesis by fabricating solar cells with thin absorber layers (ca. 150 nm). Doping of these thin layers involved ~1 min soaking. These thin solar cells also showed performance enhancement (Figures S8 and S9 and Tables S4 and S5) consistent with the picture of "p-doping" leading to the removal of the trap states that cause n-type behavior of the undoped MPA-capped QD layer. This helps us push the limits on the maximum PCE that can be achieved with an MPA-based PbS CQD solar cell.

In summary, we have successfully demonstrated a general, solution processing-enabled remote doping strategy for PbS QD solar cells employing a library of metal−organic molecules which do not require chemical bonding with the QD surface. High effective EA and low IE complexes p- and n-dope, respectively, the CQD solids. We demonstrate the advantage of remote molecular doping in the context of solar cells by utilizing a molecule with an EA larger than the ionization energy of the QDs, enabling remote electron transfer (as also suggested by DFT). We carry out an in-depth study of the effect of doping on the electronic band structure of the QDs, using UPS. Our study suggests the presence of two contrasting doping regimes: one leads to in-gap electron transfer and the second also results in the formation of large surface dipoles; the latter is deleterious to device performance. Exploiting the former, the low doping concentration regime, we effectively clean the QD band gaps, leading to a 25% increase in solar cell performance. Our mechanistic study furthers the fundamental understanding of solution processing-friendly remote molecular doping of CQD solids and presents the most versatile and scalable approach yet for achieving controlled net doping of CQD solids.

■ EXPERIMENTAL METHODS

CQD Synthesis. PbS CQDs were synthesized using a variation on a literature method,[48] employing an in-synthesis halide treatment.[43]

Dopant Synthesis. Ni(tfd)$_2$,[49] (RuCp*mes)$_2$,[36] and Mo(tfd-COCF$_3$)$_3$[31] were prepared according to the literature. The preparation of Mo(PhBz-dt)$_3$ will be published elsewhere.

Photoemission Spectroscopy. XPS measurements were carried out in an ultrahigh vacuum (UHV) Omicron chamber equipped with a SPHERA U7 hemispherical energy analyzer, employing X-ray photons having an incident kinetic energy of 1486.6 eV from a monochromated Al Kα X-ray source with a

total energy resolution of 0.1 eV. The chamber base pressure for these measurements was <5×10^{-9} mbar.

For the UPS measurements, the UHV base pressure was maintained below 8×10^{-9} mbar. The photon line width was ca. 250 eV, and the minimum spot size was ca. 1 mm. He I photons (21.2 eV) were used to acquire the spectra at normal emission. The photoelectrons were collected by the SPHERA U7 hemispherical energy analyzer with a seven-channel MCD detector, in constant analyzer energy mode. The BE values shown with 10 meV precision should be rounded to the nearest 100 meV value in accordance with the overall energy resolution.

Device Fabrication. CQD films were deposited on a TiO_2 nanoparticle-based electrode[50] on ITO-coated glass substrate using a layer-by-layer deposition approach. First, a solution of 50 mg mL^{-1} quantum dots in octane was spin-coated under ambient conditions at 2500 rpm and then followed by soaking in 1% 3-mercaptopropionic acid in methanol (v/v) for three seconds. The layer was then rinsed twice with methanol to remove the exchanged oleic acid. The process resulted in a layer with the thickness of approximately 30 nm. The process was repeated 10−12 times until the desired thickness was achieved. The CQD film was then doped, as outlined in the main text, by soaking the entire film in Mo(tfd-COCF$_3$)$_3$-containing acetonitrile solution. The top electrode was then deposited using thermal evaporation, which comprised 40 nm of MoO$_3$ and 120 nm of gold. The top electrode was deposited at the rate of 0.2 Å/s for MoO$_3$ and 1 Å/s for Au, at the pressure of 1×10^{-6} mbar.

J−V Characterization. J−V characterization was performed using a Keithley 2400 source-meter at ambient temperature, with the device in a constantly purged nitrogen environment. The solar spectrum at AM1.5 was simulated to within class A specifications (less than 25% spectral mismatch) with a xenon lamp and filters (ScienceTech; measured intensity of 100 mW cm^{-2}). The intensity of the source was calibrated using a Melles-Griot broadband powermeter and a Thorlabs broadband powermeter through a circular 0.049 cm^2 aperture at the position of the device. This was confirmed with a calibrated reference solar cell (Newport, Inc.).

Optoelectronic Device Simulations. Simulations were performed in one dimension using the SCAPS 3.0.0.1 software[51] and parameters from previous work.[45]

ASSOCIATED CONTENT

Ⓢ Supporting Information

The Supporting Information is available free of charge on the ACS Publications website at DOI: 10.1021/acsenergy-lett.6b00429.

More details on the experimental methods, XPS and UPS data, supporting device results, DFT simulations on the metal−organic complex, and photoluminescence spectroscopy results (PDF)

AUTHOR INFORMATION

Corresponding Author

*E-mail: aram.amassian@kaust.edu.sa.

Notes

The authors declare no competing financial interest.

REFERENCES

(1) Murray, C. B.; Norris, D. J.; Bawendi, M. G. Synthesis and Characterization of Nearly Monodisperse Cde (E = Sulfur, Selenium, Tellurium) Semiconductor Nanocrystallites. *J. Am. Chem. Soc.* **1993**, *115*, 8706−8715.

(2) Yin, Y.; Alivisatos, A. P. Colloidal Nanocrystal Synthesis and the Organic-Inorganic Interface. *Nature* **2005**, *437*, 664−670.

(3) Kovalenko, M. V.; Manna, L.; Cabot, A.; Hens, Z.; Talapin, D. V.; Kagan, C. R.; Klimov, V. I.; Rogach, A. L.; Reiss, P.; Milliron, D. J.; et al. Prospects of Nanoscience with Nanocrystals. *ACS Nano* **2015**, *9*, 1012−1057.

(4) Semonin, O. E.; Luther, J. M.; Choi, S.; Chen, H.-Y.; Gao, J.; Nozik, A. J.; Beard, M. C. Peak External Photocurrent Quantum Efficiency Exceeding 100% via MEG in a Quantum Dot Solar Cell. *Science* **2011**, *334*, 1530−1533.

(5) Carey, G. H.; Abdelhady, A. L.; Ning, Z.; Thon, S. M.; Bakr, O. M.; Sargent, E. H. Colloidal Quantum Dot Solar Cells. *Chem. Rev.* **2015**, *115*, 12732−12763.

(6) Wang, X.; Koleilat, G. I.; Tang, J.; Liu, H.; Kramer, I. J.; Debnath, R.; Brzozowski, L.; Barkhouse, D. A. R.; Levina, L.; Hoogland, S.; et al. Tandem Colloidal Quantum Dot Solar Cells Employing a Graded Recombination Layer. *Nat. Photonics* **2011**, *5*, 480−484.

(7) Kramer, I. J.; Sargent, E. H. The Architecture of Colloidal Quantum Dot Solar Cells: Materials to Devices. *Chem. Rev.* **2014**, *114*, 863−882.

(8) Graetzel, M.; Janssen, R. A. J.; Mitzi, D. B.; Sargent, E. H. Materials Interface Engineering for Solution-Processed Photovoltaics. *Nature* **2012**, *488*, 304−312.

(9) El-Ballouli, A. a. O.; Alarousu, E.; Kirmani, A. R.; Amassian, A.; Bakr, O. M.; Mohammed, O. F. Mohammed, O. F. Overcoming the Cut-Off Charge Transfer Bandgaps at the PbS Quantum Dot Interface. *Adv. Funct. Mater.* **2015**, *25*, 7435−7441.

(10) Chuang, C.-H. M.; Brown, P. R.; Bulović, V.; Bawendi, M. G. Improved Performance and Stability in Quantum dot Solar Cells through Band Alignment engineering. *Nat. Mater.* **2014**, *13*, 796−801.

(11) Ning, Z.; Voznyy, O.; Pan, J.; Hoogland, S.; Adinolfi, V.; Xu, J.; Li, M.; Kirmani, A. R.; Sun, J.-P.; Minor, J.; et al. Air-Stable n-Type Colloidal Quantum Dot Solids. *Nat. Mater.* **2014**, *13*, 822−828.

(12) Kramer, I. J.; Minor, J. C.; Moreno-Bautista, G.; Rollny, L.; Kanjanaboos, P.; Kopilovic, D.; Thon, S. M.; Carey, G. H.; Chou, K. W.; Zhitomirsky, D.; et al. Efficient Spray-Coated Colloidal Quantum Dot Solar Cells. *Adv. Mater.* **2015**, *27*, 116−121.

(13) Kramer, I. J.; Moreno-Bautista, G.; Minor, J. C.; Kopilovic, D.; Sargent, E. H. Colloidal Quantum Dot Solar Cells on Curved and Flexible Substrates. *Appl. Phys. Lett.* **2014**, *105*, 163902.

(14) Kim, T.; Gao, Y.; Hu, H.; Yan, B.; Ning, Z.; Jagadamma, L. K.; Zhao, K.; Kirmani, A. R.; Eid, J.; Adachi, M. M.; et al. Hybrid Tandem Solar Cells with Depleted-Heterojunction Quantum Dot and Polymer Bulk Heterojunction Subcells. *Nano Energy* **2015**, *17*, 196−205.

(15) Bozyigit, D.; Yarema, O.; Wood, V. Origins of Low Quantum Efficiencies in Quantum Dot Leds. *Adv. Funct. Mater.* **2013**, *23*, 3024−3029.

(16) Bozyigit, D.; Volk, S.; Yarema, O.; Wood, V. Quantification of Deep Traps in Nanocrystal Solids, Their Electronic Properties, and Their Influence on Device Behavior. *Nano Lett.* **2013**, *13*, 5284−5288.

(17) Bozyigit, D.; Lin, W. M. M.; Yazdani, N.; Yarema, O.; Wood, V. A Quantitative Model for Charge Carrier Transport, Trapping and Recombination in Nanocrystal-Based Solar Cells. *Nat. Commun.* **2015**, *6*, 6180.

(18) Katsiev, K.; Ip, A. H.; Fischer, A.; Tanabe, I.; Zhang, X.; Kirmani, A. R.; Voznyy, O.; Rollny, L. R.; Chou, K. W.; Thon, S. M.; et al. The Complete in-Gap Electronic Structure of Colloidal Quantum Dot Solids and Its Correlation with Electronic Transport and Photovoltaic Performance. *Adv. Mater.* **2014**, *26*, 937−942.

(19) Kirmani, A. R.; Carey, G. H.; Abdelsamie, M.; Yan, B.; Cha, D.; Rollny, L. R.; Cui, X.; Sargent, E. H.; Amassian, A. Effect of Solvent Environment on Colloidal-Quantum-Dot Solar-Cell Manufacturability and Performance. *Adv. Mater.* **2014**, *26*, 4717−4723.

(20) Kim, D.; Kim, D.-H.; Lee, J.-H.; Grossman, J. C. Impact of Stoichiometry on the Electronic Structure of PbS Quantum Dots. *Phys. Rev. Lett.* **2013**, *110*, 196802.

(21) Hwang, G. W.; Kim, D.; Cordero, J. M.; Wilson, M. W. B.; Chuang, C.-H. M.; Grossman, J. C.; Bawendi, M. G. Identifying and Eliminating Emissive Sub-Bandgap States in Thin Films of PbS Nanocrystals. *Adv. Mater.* **2015**, *27*, 4481−4486.

(22) Zhang, Y.; Zherebetskyy, D.; Bronstein, N. D.; Barja, S.; Lichtenstein, L.; Alivisatos, A. P.; Wang, L.-W.; Salmeron, M. Molecular Oxygen Induced In-Gap States in PbS Quantum Dots. *ACS Nano* **2015**, *9*, 10445−10452.

(23) Boehme, S. C.; Azpiroz, J. M.; Aulin, Y. V.; Grozema, F. C.; Vanmaekelbergh, D.; Siebbeles, L. D. A.; Infante, I.; Houtepen, A. J. Density of Trap States and Auger-Mediated Electron Trapping in Cdte Quantum-Dot Solids. *Nano Lett.* **2015**, *15*, 3056−3066.

(24) Chuang, C.-H. M.; Maurano, A.; Brandt, R. E.; Hwang, G. W.; Jean, J.; Buonassisi, T.; Bulović, V.; Bawendi, M. G. Open-Circuit Voltage Deficit, Radiative Sub-Bandgap States, and Prospects in Quantum Dot Solar Cells. *Nano Lett.* **2015**, *15*, 3286−3294.

(25) Krause, M. M.; Kambhampati, P. Linking Surface Chemistry to Optical Properties of Semiconductor Nanocrystals. *Phys. Chem. Chem. Phys.* **2015**, *17*, 18882−18894.

(26) Carey, G. H.; Chou, K. W.; Yan, B.; Kirmani, A. R.; Amassian, A.; Sargent, E. H. Materials Processing Strategies for Colloidal Quantum Dot Solar Cells: Advances, Present-Day Limitations, and Pathways to Improvement. *MRS Commun.* **2013**, *3*, 83−90.

(27) Luther, J. M.; Law, M.; Song, Q.; Perkins, C. L.; Beard, M. C.; Nozik, A. J. Structural, Optical, and Electrical Properties of Self-Assembled Films of PbSe Nanocrystals Treated with 1,2-Ethanedithiol. *ACS Nano* **2008**, *2*, 271−280.

(28) Shim, M.; Guyot-Sionnest, P. n-Type Colloidal Semiconductor Nanocrystals. *Nature* **2000**, *407*, 981−983.

(29) Rath, A. K.; Pelayo Garcia de Arquer, F.; Stavrinadis, A.; Lasanta, T.; Bernechea, M.; Diedenhofen, S. L.; Konstantatos, G. Remote Trap Passivation in Colloidal Quantum Dot Bulk Nano-Heterojunctions and Its Effect in Solution-Processed Solar Cells. *Adv. Mater.* **2014**, *26*, 4741−4747.

(30) Hassinen, A.; Moreels, I.; De Nolf, K.; Smet, P. F.; Martins, J. C.; Hens, Z. Short-Chain Alcohols Strip X-Type Ligands and Quench the Luminescence of PbSe and CdSe Quantum Dots, Acetonitrile Does Not. *J. Am. Chem. Soc.* **2012**, *134*, 20705−20712.

(31) Paniagua, S. A.; Baltazar, J.; Sojoudi, H.; Mohapatra, S. K.; Zhang, S.; Henderson, C. L.; Graham, S.; Barlow, S.; Marder, S. R. Production of Heavily n- and p-Doped CVD Graphene with Solution-Processed Redox-Active Metal-Organic Species. *Mater. Horiz.* **2014**, *1*, 111−115.

(32) Mohapatra, S. K.; Zhang, Y.; Sandhu, B.; Fonari, M. S.; Timofeeva, T. V.; Marder, S. R.; Barlow, S. Synthesis, Characterization, and Crystal Structures of Molybdenum Complexes of Unsymmetrical Electron-Poor Dithiolene Ligands. *Polyhedron* **2016**, *116*, 88−95.

(33) Qi, Y.; Sajoto, T.; Kröger, M.; Kandabarow, A. M.; Park, W.; Barlow, S.; Kim, E.-G.; Wielunski, L.; Feldman, L. C.; Bartynski, R. A.; et al. A Molybdenum Dithiolene Complex as p-Dopant for Hole-Transport Materials: A Multitechnique Experimental and Theoretical Investigation. *Chem. Mater.* **2010**, *22*, 524−531.

(34) Connelly, N. G.; Geiger, W. E. Chemical Redox Agents for Organometallic Chemistry. *Chem. Rev.* **1996**, *96*, 877−910.

(35) Qi, Y.; Sajoto, T.; Barlow, S.; Kim, E.-G.; Brédas, J.-L.; Marder, S. R.; Kahn, A. Use of a High Electron-Affinity Molybdenum Dithiolene Complex to p-Dope Hole-Transport Layers. *J. Am. Chem. Soc.* **2009**, *131*, 12530−12531.

(36) Mohapatra, S. K.; Fonari, A.; Risko, C.; Yesudas, K.; Moudgil, K.; Delcamp, J. H.; Timofeeva, T. V.; Brédas, J.-L.; Marder, S. R.; Barlow, S. Dimers of Nineteen-Electron Sandwich Compounds: Crystal and Electronic Structures, and Comparison of Reducing Strengths. *Chem. - Eur. J.* **2014**, *20*, 15385−15394.

(37) Guo, S.; Kim, S. B.; Mohapatra, S. K.; Qi, Y.; Sajoto, T.; Kahn, A.; Marder, S. R.; Barlow, S. n-Doping of Organic Electronic Materials Using Air-Stable Organometallics. *Adv. Mater.* **2012**, *24*, 699−703.

(38) Kirmani, A. R.; Peng, W.; Mahfouz, R.; Amassian, A.; Losovyj, Y.; Idriss, H.; Katsiev, K. On the Relation between Chemical Composition and Optical Properties of Detonation Nanodiamonds. *Carbon* **2015**, *94*, 79−84.

(39) Katsiev, K.; Losovyj, Y.; Zhou, Z.; Vescovo, E.; Liu, L.; Dowben, P. A.; Goodman, D. W. Graphene on Ru(0001): Evidence for Two Graphene Band Structures. *Phys. Rev. B: Condens. Matter Mater. Phys.* **2012**, *85*, 195405.

(40) Miller, E. M.; Kroupa, D. M.; Zhang, J.; Schulz, P.; Marshall, A. R.; Kahn, A.; Lany, S.; Luther, J. M.; Beard, M. C.; Perkins, C. L.; et al. Revisiting the Valence and Conduction Band Size Dependence of PbS Quantum Dot Thin Films. *ACS Nano* **2016**, *10*, 3302−3311.

(41) Tarasov, A.; Zhang, S.; Tsai, M.-Y.; Campbell, P. M.; Graham, S.; Barlow, S.; Marder, S. R.; Vogel, E. M. Controlled Doping of Large-Area Trilayer MoS_2 with Molecular Reductants and Oxidants. *Adv. Mater.* **2015**, *27*, 1175−1181.

(42) Brown, P. R.; Kim, D.; Lunt, R. R.; Zhao, N.; Bawendi, M. G.; Grossman, J. C.; Bulović, V. Energy Level Modification in Lead Sulfide Quantum Dot Thin Films through Ligand Exchange. *ACS Nano* **2014**, *8*, 5863−5872.

(43) Ip, A. H.; Thon, S. M.; Hoogland, S.; Voznyy, O.; Zhitomirsky, D.; Debnath, R.; Levina, L.; Rollny, L. R.; Carey, G. H.; Fischer, A.; et al. Hybrid Passivated Colloidal Quantum Dot Solids. *Nat. Nanotechnol.* **2012**, *7*, 577−582.

(44) Ning, Z.; Zhitomirsky, D.; Adinolfi, V.; Sutherland, B.; Xu, J.; Voznyy, O.; Maraghechi, P.; Lan, X.; Hoogland, S.; Ren, Y.; et al. Graded Doping for Enhanced Colloidal Quantum Dot Photovoltaics. *Adv. Mater.* **2013**, *25*, 1719−1723.

(45) Zhitomirsky, D.; Voznyy, O.; Levina, L.; Hoogland, S.; Kemp, K. W.; Ip, A. H.; Thon, S. M.; Sargent, E. H. Engineering Colloidal Quantum Dot Solids within and Beyond the Mobility-Invariant Regime. *Nat. Commun.* **2014**, *5*, 3803.

(46) Koh, W.-k.; Koposov, A. Y.; Stewart, J. T.; Pal, B. N.; Robel, I.; Pietryga, J. M.; Klimov, V. I. Heavily Doped N-Type Pbse and Pbs Nanocrystals Using Ground-State Charge Transfer from Cobaltocene. *Sci. Rep.* **2013**, *3*, 2004.

(47) Maraghechi, P.; Labelle, A. J.; Kirmani, A. R.; Lan, X.; Adachi, M. M.; Thon, S. M.; Hoogland, S.; Lee, A.; Ning, Z.; Fischer, A.; et al. The Donor−Supply Electrode Enhances Performance in Colloidal Quantum Dot Solar Cells. *ACS Nano* **2013**, *7*, 6111−6116.

(48) Hines, M. A.; Scholes, G. D. Colloidal Pbs Nanocrystals with Size-Tunable near-Infrared Emission: Observation of Post-Synthesis Self-Narrowing of the Particle Size Distribution. *Adv. Mater.* **2003**, *15*, 1844−1849.

(49) Harrison, D. J.; Nguyen, N.; Lough, A. J.; Fekl, U. New Insight into Reactions of $Ni(S_2C_2(CF_3)_2)_2$ with Simple Alkenes: Alkene Adduct Versus Dihydrodithiin Product Selectivity Is Controlled by $[Ni(S_2C_2(CF_3)_2)_2]^-$ Anion. *J. Am. Chem. Soc.* **2006**, *128*, 11026−11027.

(50) Ip, A. H.; Kiani, A.; Kramer, I. J.; Voznyy, O.; Movahed, H. F.; Levina, L.; Adachi, M. M.; Hoogland, S.; Sargent, E. H. Infrared Colloidal Quantum Dot Photovoltaics Via Coupling Enhancement and Agglomeration Suppression. *ACS Nano* **2015**, *9*, 8833−8842.

(51) Burgelman, M.; Decock, K.; Khelifi, S.; Abass, A. Advanced Electrical Simulation of Thin Film Solar Cells. *Thin Solid Films* **2013**, *535*, 296−301.